



Interfacial defect passivation and stress release by multifunctional KPF₆ modification for planar perovskite solar cells with enhanced efficiency and stability

Huan Bi, Baibai Liu, Dongmei He, Le Bai, Wenqi Wang, Zhigang Zang ^{*}, Jiangzhao Chen ^{*}

Key Laboratory of Optoelectronic Technology & Systems (Ministry of Education), College of Optoelectronic Engineering, Chongqing University, Chongqing 400044, China



ARTICLE INFO

Keywords:
Perovskite solar cells
Interface engineering
Multifunctional
Defect passivation
Stress release

ABSTRACT

Interfacial defect and residual stress hinder the further enhancement of power conversion efficiency (PCE) and stability of perovskite solar cells (PSCs). Here, we report a multifunctional interface modification strategy where KPF₆ molecule is employed to modify SnO₂/perovskite interface. It is revealed that PF₆⁻ is still located at interface whereas most of K⁺ ions diffuse into perovskite layer. PF₆⁻ can chemically link SnO₂ layer and perovskite layer via the hydrogen bond with perovskites and coordination bond with SnO₂, resulting in improved interfacial contact. KPF₆ interface modification leads to improved perovskite film quality, interfacial defect passivation, and interfacial stress release. As a result, the KPF₆-modified device achieves an efficiency enhancement from 19.66% to 21.39% as compared to the control device. Meanwhile, moisture, thermal and light stability are ameliorated after interface modification. The unencapsulated KPF₆-modified device maintains 80.1% of its initial PCE after aging for 960 h at 60 °C and 57.2% after aging for 960 h under one sun illumination, respectively. This work provides an idea for developing multifunctional interface molecules toward simultaneously enhancing efficiency and stability of PSCs.

1. Introduction

The perovskite solar cells (PSCs) have witnessed a rapid development in power conversion efficiency (PCE) and stability since the first report on the all-solid-state PSCs with a promising PCE of 9.7% [1]. Recently, the certified record PCE of single-junction PSCs has reached 25.5% [2], which is approaching that of monocrystalline silicon solar cells. Currently, most of high-efficiency PSCs with a PCE exceeding 24% were fabricated based on mesoporous TiO₂ electron transport layer (ETL) [3–5]. However, the fabrication of mesoporous TiO₂ ETL requires high annealing temperature, which is energy-intensive and not compatible with the fabrication of flexible PSCs. Moreover, TiO₂ based PSCs are usually perplexed by the poor ultraviolet stability and serious hysteresis. In recent several years, tin dioxide (SnO₂) based PSCs have received significant attention due to low-temperature fabrication, excellent ultraviolet stability and low hysteresis [6–9]. Currently, the highest PCE of as high as 25.2% has been achieved for SnO₂ based PSCs [6]. Nevertheless, this efficiency value is still far from the theoretical Shockley–Queisser limit efficiency [10]. Poor perovskite film quality, interfacial defects, and interfacial stress should be mainly responsible for the

efficiency and stability losses [10–15]. Consequently, it is imperative to further increase efficiency and stability of SnO₂ based PSCs through improving perovskite film quality, passivating interfacial defects, and releasing interfacial stress.

The perovskite film quality is directly related to the PCE and stability of the final PSCs. Presently, all efficient PSCs were fabricated based on polycrystalline perovskite film instead of single crystal one [3–6,8,15–16]. However, a mass of defects would be inevitably produced in the final polycrystalline perovskite film during high-temperature annealing and fast crystallization, which would result in nonradiative recombination loss and thus deteriorate device performance [10,17]. It is well-known that the quality of perovskite films can be regulated through the following strategies, such as perovskite composition engineering, precursor solvent and antisolvent engineering, additive engineering, deposition substrate modulation, etc. Among them, it has been demonstrated to be one of feasible and effective approaches to improve perovskite film quality via modulating deposition substrate [9,18]. Except for perovskite film quality, interfacial nonradiative recombination resulting from interfacial defects from the surfaces of perovskite and/or charge transport layer is one of important

* Corresponding authors.

E-mail addresses: zanggz@cqu.edu.cn (Z. Zang), jiangzhaochen@cqu.edu.cn (J. Chen).

reasons for device performance loss. It was widely testified that the SnO_2 /perovskite interface plays a critical role in the final device performance [19–22]. The positively charged defects (e.g., oxygen vacancies, and halide vacancies) and negatively charged defects (e.g., cation vacancies, and Pb-I antisites) may exist simultaneously at this interface. Compared with TiO_2 /perovskite interface, the work on modulating SnO_2 /perovskite interface is highly limited [11]. To date, some molecules have been developed to passivate the interfacial defects at SnO_2 /perovskite interface, such as Lewis acid or base [23–24], anion [25] or cation [26–27], organic or inorganic salts [19,28], etc. Among them, salt molecules containing both anion and cation could be more effective owing to the simultaneous passivation of anionic and cationic defects [19,28]. However, rational engineering of anion and cation is of great importance in order to maximize the passivation effect of the salt molecules. In the past few years, potassium ion (K^+) has been extensively demonstrated to be able to effectively passivate the defects in perovskite films and accordingly to increase device performance [29–32]. To the best of our knowledge, most of salt interface modifiers employed halide anions as counterions up to now [8,19,28]. To seek out the optimal anions, molecular anions also should be attempted. For this purpose, an enhancement from 17.8% to 19.3% was achieved due to the formation of $\text{FA}_{0.88}\text{Cs}_{0.12}\text{PbI}_{3-x}(\text{PF}_6)_x$ interlayer at perovskite/Spiro-OMeTAD interface by ion exchange reaction between I^- and PF_6^- [33]. It was found that formed interlayer can effectively passivate the defects at the surface of perovskite films. In addition, some other molecular anions were also incorporated into interface modifiers to passivate interfacial defects, such as BF_4^- [34], SO_4^{2-} [35], NO_3^- [36], etc. Consequently, molecular anions are expected to be incorporated into interface molecules to further increase the efficiency and stability of PSCs.

In recent two years, stress-induced strain in perovskite films has been demonstrated to be detrimental to device performance [37]. The stress (σ) can be estimated according to the formula of $\sigma_{\Delta T} = E_p/(1 - \nu_p)(\alpha_s - \alpha_p)\Delta T$, where E_p is the modulus of the perovskite, ν_p is Poisson's ratio of the perovskite, α_s and α_p are the thermal expansion coefficients of the substrate and the perovskite, respectively, and ΔT is the temperature gradient [38]. Therefore, generation of stress in perovskite films is mainly ascribed to the thermal expansion coefficients difference of the substrate and the perovskite, temperature gradient, and E_p . Since high-temperature annealing is indispensable for high-quality perovskite films, it could be an effective method of releasing interfacial stress to reduce E_p and thermal expansion coefficients difference via modulating SnO_2 /perovskite interface. In view of this, Wang et al. released the interfacial stress through treating perovskite films with organic ammonium salts (octylammonium iodide (OAI) and phenethylammonium iodide (PEAI)), which was attributed to the lattice reconstruction at the surface of the perovskite films and thus reduced elastic modulus [39]. Xue et al. found that the residual tensile strain can be compensated by incorporating an external compressive strain from hole transport layer [38]. Additionally, the tensile stress was released through inserting WS_2 interface layer between $\text{SnO}_2\text{-TiO}_{x\text{Cl}}_{4-2x}$ ETL and CsPbBr_3 , led to improved efficiency and stability [40]. The above works strongly suggest that it is a feasible and effective method to release interfacial stress by interface engineering.

To date, most interface modification molecules either improve perovskite film quality, passivate interfacial defects, or release interfacial stress. It is still a big challenge to simultaneously achieve the above three functions. We previously developed a multifunctional chemical linker 4-imidazoleacetic acid hydrochloride (ImAcHCl) to modify the SnO_2 /perovskite interface, resulting in the realization of crystallization improvement, defect passivation, and energy level alignment modulation [19]. In addition, You et al. achieved an average PCE of 23.03% through a multifunctional modification strategy where a biological polymer (HP) was employed to modify SnO_2 nanocrystals [9]. The above works encourage us to develop more effective interface modification molecules to improve perovskite film quality, passivate interfacial defects, and release interfacial stress simultaneously.

In this work, we developed a multifunctional interface modification strategy where potassium hexafluorophosphate (KPF_6) is incorporated to modify SnO_2 /perovskite interface. After KPF_6 modification, multiple functions have been realized, including facilitating perovskite crystallization, passivating interfacial defects, and releasing interfacial stress. As a result, both PCE and stability are enhanced after KPF_6 modification. The device modified by KPF_6 achieves a PCE of 21.39%. The unencapsulated modified device maintains 80.1% of their initial PCE after aging at 60 °C for 960 h and 57.2% after aging under one sun illumination for 960 h, respectively.

2. Results and discussion

The planar PSC with the structure of ITO/ SnO_2 /perovskite/Spiro-OMeTAD/Au was fabricated, where perovskite composition was $\text{Rb}_{0.05}(\text{FA}_{0.95}\text{MA}_{0.05})_{0.95}\text{PbI}_{2.85}\text{Br}_{0.15}$. In order to further improve the PCE and stability of SnO_2 based PSCs, we introduced KPF_6 to modify SnO_2 /perovskite interface, as shown in Fig. 1a. As reported previously, K^+ is expected to be capable of passivating cation vacancy defects from the terminal of perovskite films or suppressing iodide ion migration [29–31]. PF_6^- is expected to be able to chemically link perovskite layer and SnO_2 layer. On the one hand, the strong hydrogen bond would be formed between F atom in PF_6^- and organic cations (i.e., formamidinium (FA^+) and methylammonium (MA^+)) from perovskite. On the other hand, the coordination bond would be formed between F atom in PF_6^- and Sn^{4+} in SnO_2 (oxygen vacancies).

First, time of flight secondary ion mass spectroscopy (ToF-SIMS) measurement was performed to confirm the presence of the KPF_6 and investigate its cross-sectional distribution. As illustrated in Fig. 1b, appearance of F^- and K^+ ions confirmed the existence of KPF_6 in the final device. It was interesting that F^- ions were still located at the SnO_2 /perovskite interface while most of K^+ ions had diffused into the whole of perovskite films to form a gradient distribution from the surface of perovskite films to bottom interface. This indicates that K^+ ions can freely migrate probably because of no chemical interaction while F^- ions were bound at SnO_2 /perovskite interface due to some kind of strong chemical interaction. X-ray photoelectron spectroscopy (XPS) and Fourier transforms infrared spectroscopy (FTIR) measurements were further carried out to study the chemical interaction between KPF_6 and perovskite or SnO_2 . The XPS survey spectra of the pristine SnO_2 and the KPF_6 -modified SnO_2 are shown in Fig. S1. As illustrated in Fig. 1c, the binding energies of $\text{Sn } 3d_{5/2}$ (486.8 eV) and $3d_{3/2}$ (495.3 eV) peaks of SnO_2 film were increased to 487.1 eV and 495.6 eV after KPF_6 modification, respectively, which showed that there was a strong chemical interaction between SnO_2 and KPF_6 . A new peak at 487.9 eV in KPF_6 -modified SnO_2 was observed, which was assigned to the formation of Sn-F bond [41]. There was $\text{F } 1s$ peak in the KPF_6 -modified SnO_2 sample while no $\text{F } 1s$ peak in the pristine SnO_2 sample, which again confirmed the presence of KPF_6 in final device, as presented in Fig. 1d. Interestingly, two $\text{F } 1s$ peaks (684.5 eV and 687.4 eV) were obviously observed, which were assigned to F in PF_6^- and F in Sn-F bond, respectively. It indicates that the chemical interaction between SnO_2 and KPF_6 occurred via the coordination bond between F in PF_6^- and SnO_2 . As exhibited in O 1s spectra in Fig. 1e, the O 1s peak of both SnO_2 and modified SnO_2 films was deconvoluted into two peaks of 529.9 eV and 531.8 eV, which was ascribed to lattice oxygen (O_L) and vacancy oxygen (O_V) in SnO_2 , respectively [42]. The peak area ratio (R_{OV}) of O_V was estimated by the formula of $R_{\text{OV}} = \text{S}_{\text{OV}}/(\text{S}_{\text{OL}} + \text{S}_{\text{OV}})$, where S_{OV} and S_{OL} stand for the peak area of O_V and O_L , respectively. The R_{OV} of SnO_2 with KPF_6 was calculated to be 0.27, which was lower than 0.32 of the pristine SnO_2 . This means that oxygen vacancies were effectively filled by F in KPF_6 . It was reported that oxygen vacancy defects in SnO_2 ETL were harmful to device performance [42]. As displayed in Fig. 1f, new peak at 552 cm^{-1} due to the stretching vibration of Sn-F [43] was found in the KPF_6 -modified SnO_2 as compared to bare SnO_2 , confirming the chemical interaction between PF_6^- and SnO_2 , which was consistent with the XPS

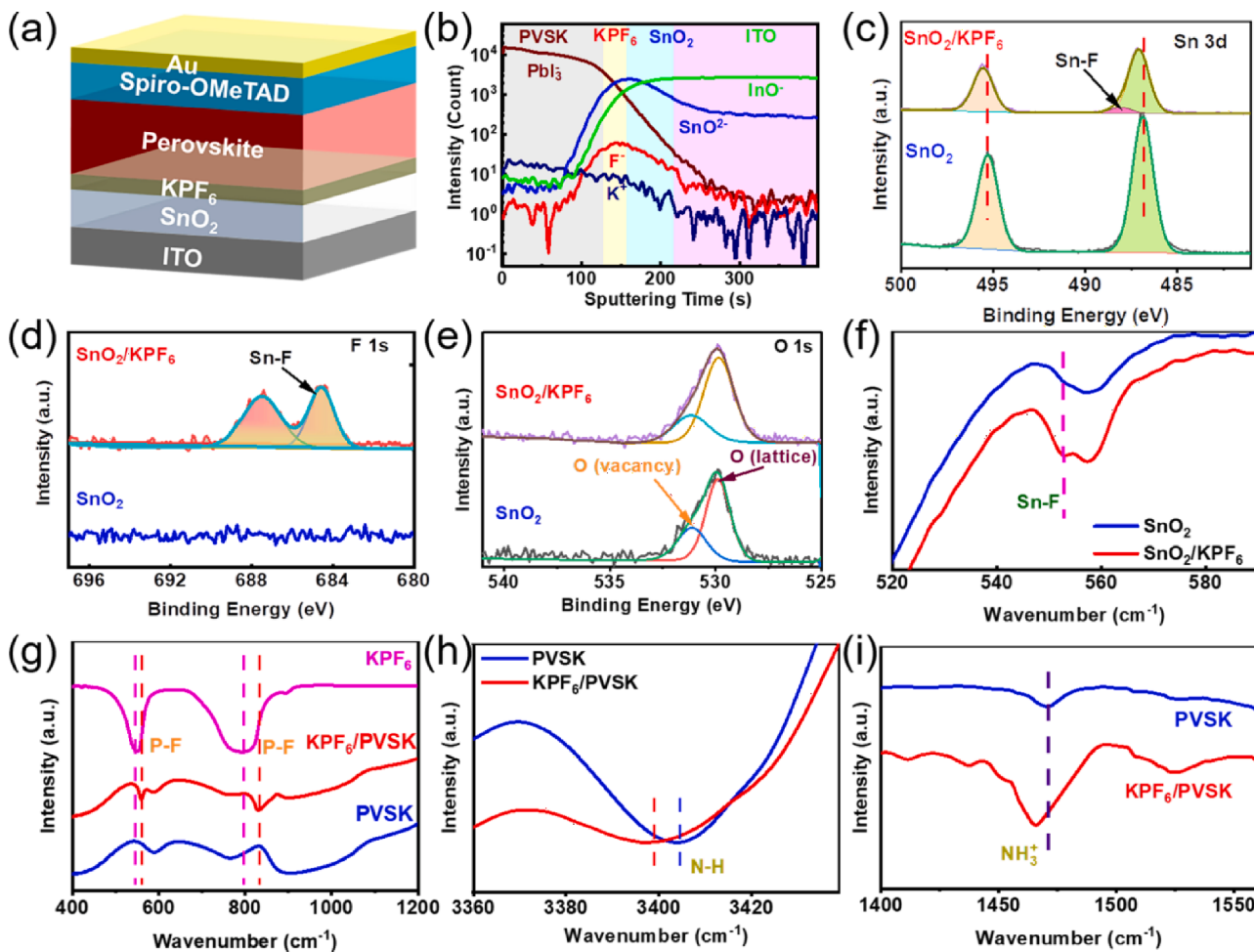


Fig. 1. (a) Schematic illustration of the device structure in this work. (b) ToF-SIMS depth profiles of the perovskite/KPF₆/SnO₂/ITO/glass. The molecular fragments from the perovskite (Pbl₃), KPF₆ (F⁻ and K⁺), the SnO₂ (SnO²⁻), and the ITO (InO⁻) are shown. (c) Sn 3d, (d) F 1 s, and (e) O 1 s XPS spectra of the SnO₂ films without and with KPF₆ modification. (f) FTIR spectra of the SnO₂ films without and with KPF₆ modification. FTIR spectra in the range of (g) 400–1200 cm⁻¹, (h) 3360–3440 cm⁻¹, and i) 1400–1560 cm⁻¹ of KPF₆, glass/perovskite, and glass/KPF₆/perovskite. PVSK stands for perovskite.

results in Fig. 1c-e. The two peaks (546.2 cm⁻¹ and 793.1 cm⁻¹) from P-F in pure KPF₆ were shifted to higher wavenumbers in comparison with the SnO₂ with KPF₆ (560.2 cm⁻¹ and 828.3 cm⁻¹), as illustrated in Fig. 1g. The peak at 3404.3 cm⁻¹ assigned to N—H stretching vibration in pristine perovskite was shifted toward higher wavenumber compared with the perovskite with KPF₆ (3398.0 cm⁻¹) (Fig. 1h). [44] Moreover, the peak wavenumber of NH₃⁺ was reduced from 1471.1 cm⁻¹ of bare perovskite film to 1465.7 cm⁻¹ of the KPF₆-modified perovskite film (Fig. 1i) [45]. The above results suggest that the hydrogen bond between PF₆⁻ in KPF₆ and NH₃⁺ in perovskite was formed. In a word, PF₆⁻ in KPF₆ can chemically link perovskite layer and SnO₂ layer through hydrogen bond and coordination bond, respectively.

UV-vis absorption measurement was carried out to investigate the effect of the KPF₆ modification on the light harvesting property of perovskite films. Obviously, the absorption intensity was almost not affected by KPF₆ modification as revealed in Fig. S2. As shown in Atomic force microscopy (AFM) images in Fig. S3, the root means square (RMS) roughness of perovskite film was reduced from 29 nm to 21 nm after KPF₆ modification. The top-view and cross-sectional scanning electron microscopy (SEM) images of the perovskite films deposited on the glass/ITO/SnO₂ without and with KPF₆ modification are exhibited in Fig. 2a-d. We can clearly see some pinholes in the control perovskite film while no in the modified one (Fig. 2a,b). More uniform and smoother perovskite film was obtained after KPF₆ modification as compared to the control perovskite film. The cross section of the perovskite film with

KPF₆ seems to be smoother and more compact than that of the control perovskite film (Fig. 2c,d). The perovskite film with KPF₆ modification had a larger average grain size of 1.55 μm compared to the control perovskite film (1.37 μm) (Fig. 2e,f). In short, KPF₆ modification improved perovskite film quality by increasing grain size and improving morphology. It implies that KPF₆ can facilitate perovskite growth.

The steady-state photoluminescence (SSPL) and time-resolved photoluminescence (TRPL) spectra were measured to uncover the effect of KPF₆ interface modification on the carrier lifetimes of perovskite films (Fig. 3a,b). TRPL spectra were fitted by using the double exponential function equation of $I(t) = I_0 + A_1 \exp(-t/\tau_1) + A_2 \exp(-t/\tau_2)$ [19,46], where A_1 and A_2 represent the decay amplitude of fast and slow decay process, respectively. τ_1 and τ_2 stand for the fast and slow decay time constants, respectively. The average carrier lifetime (τ_{ave}) was calculated through employing the equation of $\tau_{ave} = (A_1\tau_1^2 + A_2\tau_2^2)/(A_1\tau_1 + A_2\tau_2)$ [19,46]. The corresponding fitting data are shown in Table S1. As presented in Fig. 3a, PL intensity of the perovskite film with KPF₆ was much higher than that of the control perovskite film regardless of measuring direction (glass side or perovskite side), which was in good agreement with the significant carrier lifetimes from 1347.6 ns to 2547.5 ns upon measuring from glass side and from 1539.7 ns to 2155.2 ns measuring from perovskite side (Fig. 3b and Table S1). Regarding perovskite side, K⁺ diffused from KPF₆ at interface could passivate the defects within perovskite films. The improved perovskite film quality was also one of reasons for increased carrier lifetimes. With respect to

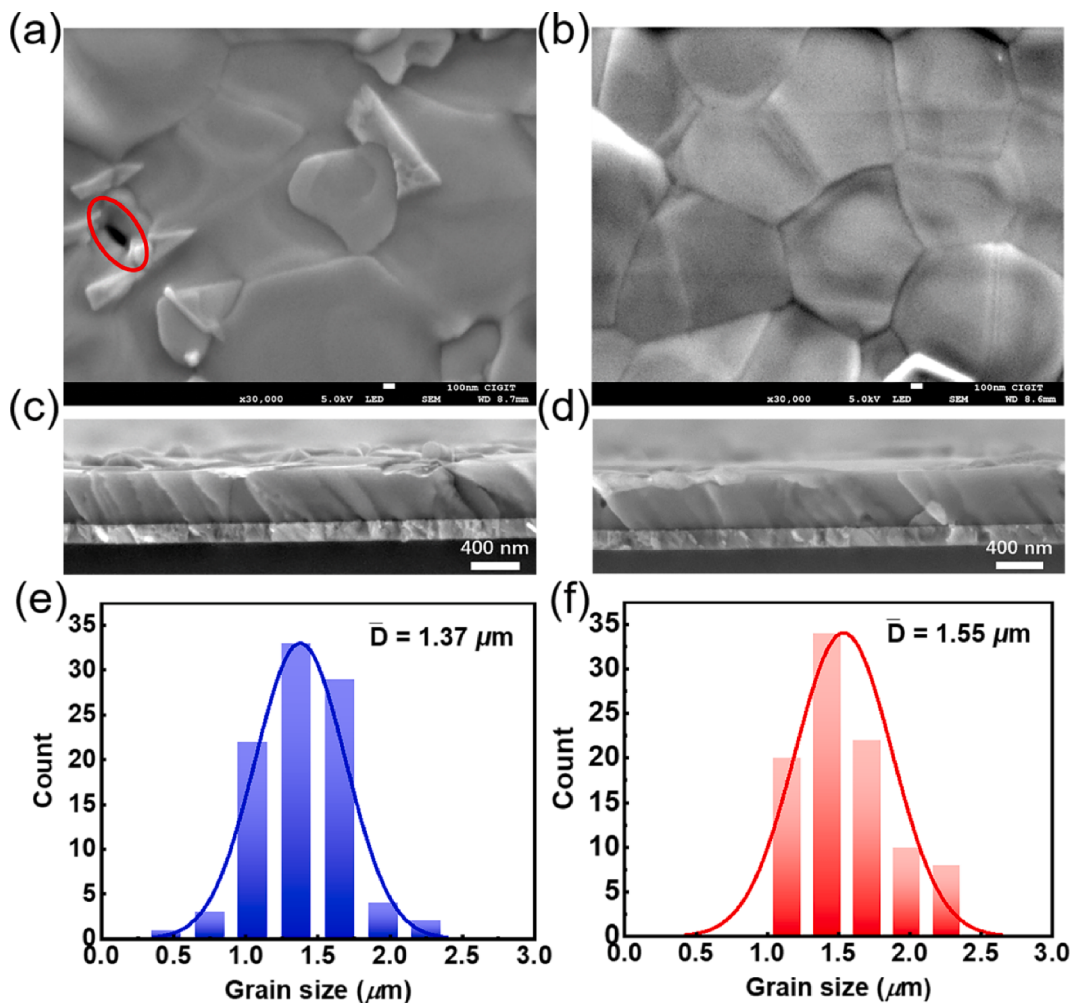


Fig. 2. Top-view SEM images of the perovskite films prepared on (a) SnO₂ and (b) SnO₂ modified by KPF₆ films. Cross-sectional SEM images of (c) ITO/SnO₂/perovskite and (d) ITO/ SnO₂/KPF₆/perovskite samples. The scale bar is 400 nm. The corresponding grain size statistics from (a) and (b) are shown in (e) and (f), respectively.

the glass side, the enhanced carrier lifetimes should be ascribed to effective passivation of KPF₆ for the defects from perovskite films. Besides, increase degree in PL intensity and carrier lifetimes from glass side was larger than that from perovskite side. It shows that KPF₆ modification had a bigger effect on interface relative to bulk of perovskite films. Interestingly, slightly blue-shifted PL peaks can be observed after KPF₆ modification independent of measuring directions, which also confirmed that KPF₆ can effectively passivate interfacial trap states [47,48]. As exhibited in PL mapping images in Fig. 3d,e, PL intensity was remarkably increased after KPF₆ modification, which was in excellent accordance with the above single-point PL measurement results.

Subsequently, the space charge limited current (SCLC) measurement was performed to quantitatively calculate the defect densities of perovskite films without and with KPF₆. Fig. 3e,f show the typical dark current–voltage (*I*-*V*) curves of electron-only devices (ITO/SnO₂/perovskite/PCBM/BCP/Ag and ITO/SnO₂/KPF₆/perovskite/PCBM/BCP/Ag). The defect density was calculated according to the equation of $n_t = (2\epsilon\epsilon_0 V_{TFL})/(eL^2)$, where ϵ is the dielectric constant of the perovskite, ϵ_0 is the vacuum dielectric constant, V_{TFL} is trap-filled limit voltage obtained by fitting dark *I*-*V* curves, L is the thickness film of the perovskite, and e is the elementary charge [19]. KPF₆ modification led to significant decrease in defect density from $9.01 \times 10^{15} \text{ cm}^{-3}$ to $3.38 \times 10^{15} \text{ cm}^{-3}$, which was consistent with increased carrier lifetimes (Fig. 3b and Table S1). Both PL and defect density measurements indicate that

KPF₆ modification can markedly improve perovskite film quality through increasing carrier lifetimes and reducing defect density. The improved film quality could be attributed to the following reasons: First, K⁺ ions that diffused from interface into bulk of perovskite film could effectively passivate the defects within the perovskite films. Second, improved perovskite crystallization due to KPF₆ modification should contribute to the improved film quality. Third, iodine vacancy defects could be filled by PF₆⁻. Finally, the FA⁺ or MA⁺ vacancies may be reduced due to effective inhibition of organic cation migration through forming strong hydrogen bond between PF₆⁻ and NH₃⁺.

X-ray diffraction (XRD) measurement was carried out to gain insights into the effect of KPF₆ modification on crystal structure and crystallinity of the perovskite films, as shown in Fig. 4a. The characteristic diffraction peaks at 2θ values of 13.97°, 28.19°, 31.58°, 40.29°, and 42.78°, corresponding to the (101), (202), (211), (024) and (131) crystal planes of cubic perovskite, respectively, were observed in both control and modified perovskite films. This means that KPF₆ modification did not change the crystal structure of perovskite films. The crystallinity of the perovskite film was increased after KPF₆ modification as reflected by the enhanced diffraction peak intensity. As we discussed in the introduction, interfacial residual stress was detrimental to device performance. The depth-dependent grazing incident X-ray diffraction (GIXRD) measurement has been successfully used to investigate the stress distribution of perovskite films [40]. Here we also used depth-dependent GIXRD measurement to reveal the effect of KPF₆ modification on interfacial

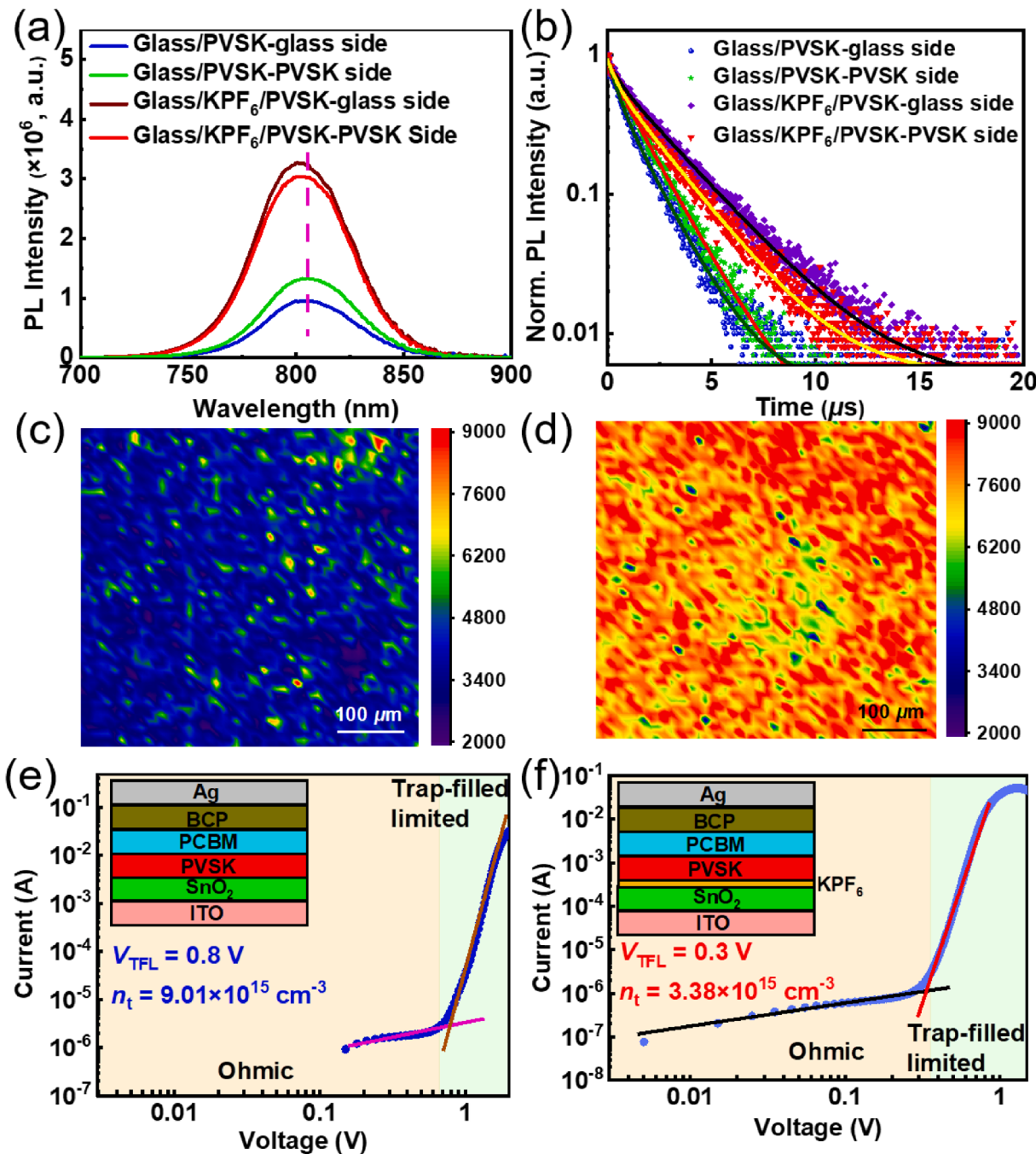


Fig. 3. (a) Steady-state photoluminescence (SSPL) and (b) Time-resolved photoluminescence (TRPL) spectra of the perovskite films deposited on non-conductive glass and KPF₆-coated non-conductive glass, which were measured from the glass side or perovskite side. PVK stands for perovskite. PL mapping images of the perovskite films prepared on the (c) glass and (d) glass/KPF₆ substrates. Dark I-V curves of the electron-only devices with the structures of (e) ITO/SnO₂/perovskite/PCBM/BCP/Ag and (f) ITO/SnO₂/KPF₆/perovskite/PCBM/BCP/Ag.

residual stress, as displayed in Fig. S4. First, it is important for finding a suitable incident angle (ω) to ensure that the SnO₂/perovskite interface can be detected. As shown in Fig. S5, a characteristic diffraction peak of SnO₂ was observed upon $\omega = 1.5^\circ$ whereas no this peak upon $\omega = 1.3^\circ$. Therefore, we selected a series of ω ($\omega = 0.3^\circ, 0.5^\circ, 0.7^\circ, 0.9^\circ, 1.1^\circ, 1.3^\circ$, and 1.5°) to explore the stress distribution of perovskite films at different depths. The diffraction peak at $2\theta = 31.58^\circ$ of the control perovskite film gradually shifted toward low angles as the ω increased from 0.3° to 1.5° while the diffraction peak of the perovskite film modified by KPF₆ was almost maintained regardless of ω (Fig. 4b,c). According to the Bragg equation of $n\lambda = 2ds\sin\theta$, the shift of diffraction peak toward low angle would result in increased interplanar crystal spacing and thus lattice

expansion, finally leading to stress and strain. Evidently increased d -spacing of the unmodified perovskite film was observed upon varying the incident angles from 0.3° to 1.5° while the d -spacing of the modified perovskite film was almost maintained constant, as shown in Fig. 4d. This suggested that the residual stress of perovskite films was almost released completely after KPF₆ modification. The released stress could be related to effective interfacial defect passivation after KPF₆ modification. It was reported that interfacial stress was effectively released through incorporating WS₂ at ETL/CsPbBr₃ interface [40]. They thought that WS₂ acted as “lubricant” between ETL and perovskite. In our work, KPF₆ could serve as the similar function with the above work because KPF₆ can chemically link SnO₂ ETL and perovskite layer as well

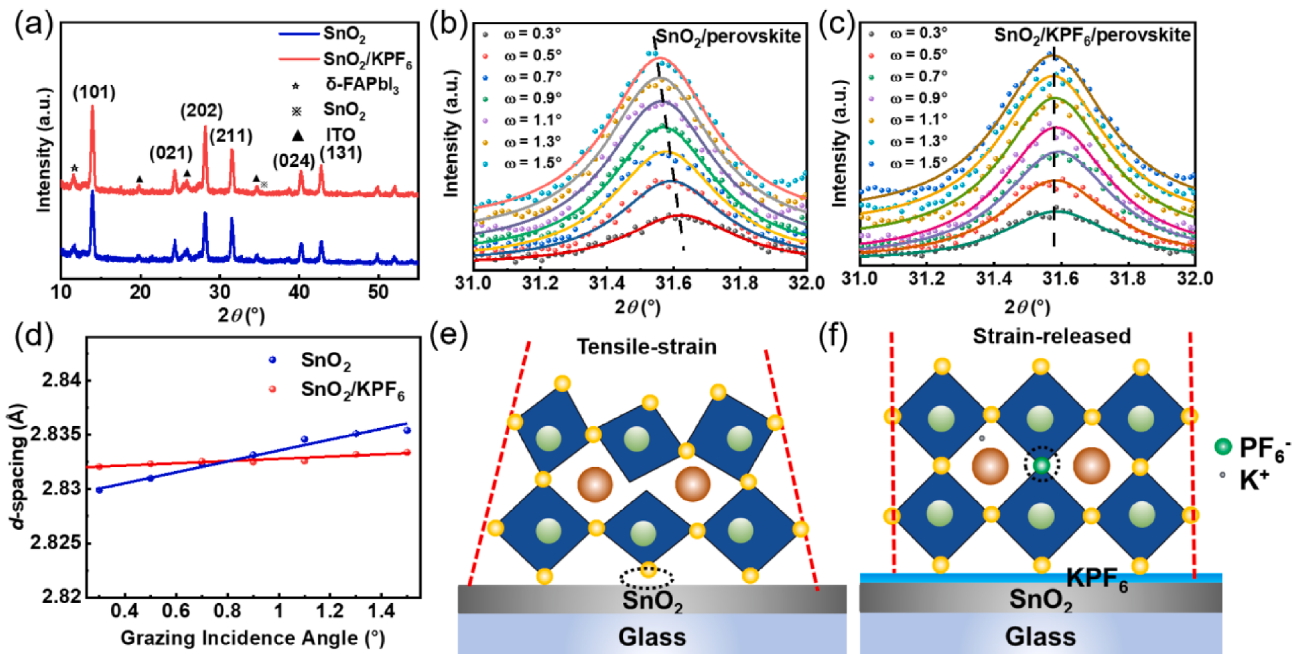


Fig. 4. (a) XRD patterns of the perovskite films based on SnO₂ with or without KPF₆. Depth-dependent GIXRD patterns of the perovskite films based on (b) SnO₂ and (c) SnO₂/KPF₆. (d) d-spacing values obtained from (211) plane as a function of incidence angle. Schematic illustration of residual stress of the perovskite films prepared on (e) SnO₂ and (f) KPF₆-modified SnO₂.

as passivate interfacial defects. Schematic illustration of residual stress of the perovskite films prepared on SnO₂ and KPF₆-modified SnO₂ is exhibited in Fig. 4e,f. The residual tensile stress was observed in the control perovskite film whereas the residual stress was released in the KPF₆-modified one. In addition, it was revealed that the crystallinity was improved at different depths as supported by the smaller full width at half maxima (FWHM) of the diffraction peaks corresponding to (211)

crystal plane of the perovskite films with KPF₆ as compared to the control perovskite film (Fig. S6).

Steady-state photoluminescence (SSPL) and time-resolved photoluminescence (TRPL) spectra were measured to help us to further understand the dynamics of interfacial charge extraction of the PSCs without or with KPF₆ (Fig. 5a, b and Table S2). Reduced PL intensity and carrier lifetimes from 1384.4 ns to 960.3 ns confirmed that electron

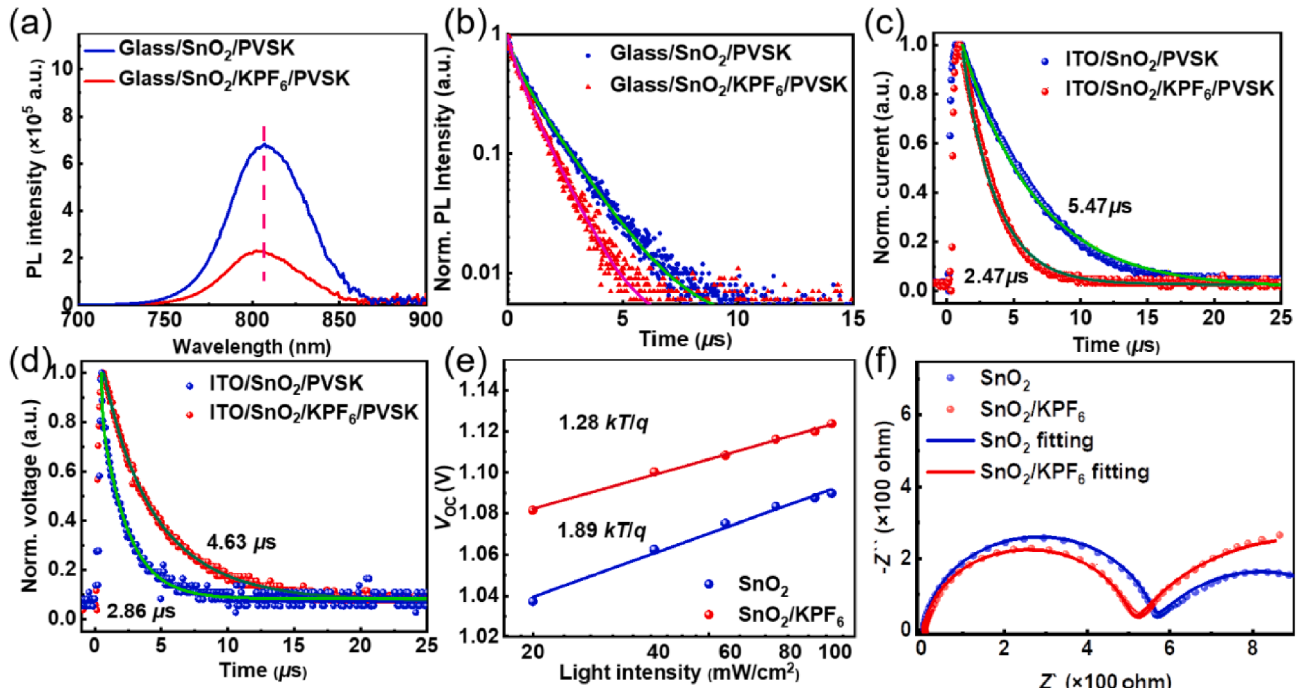


Fig. 5. (a) SSPL and (b) TRPL spectra of the perovskite films deposited on glass, SnO₂, and SnO₂/KPF₆ substrates. (c) Transient photocurrent and d) transient photovoltage curves of the PSCs based on SnO₂ and SnO₂ with KPF₆. (e) V_{OC} as a function of light intensities for the devices based on SnO₂ and KPF₆-modified SnO₂. (f) Nyquist plots of the PSCs based on SnO₂ and SnO₂ with KPF₆ modification which was measured at a bias of 0.9 V in the frequency range of 1 MHz to 0.1 Hz under one sun illumination.

extraction was improved after KPF_6 modification. Capacitance-voltage ($C-V$) measurement is performed to further study the interfacial charge transfer and extraction. As presented in Fig. S7, increased built-in potential (V_{bi}) was found for the KPF_6 modified device as compared to the control device, which was beneficial for charge transfer and extraction [11]. As shown in Fig. 5c, the device with KPF_6 modification (2.47 μs) possessed a shorter carrier extraction lifetime as compared to the control device (5.47 μs) as revealed by transient photocurrent (TPC), which was indicative of a much better charge transfer and extraction. Transient photovoltage (TPV) results showed that carrier lifetime was increased from 2.86 μs to 4.63 μs after KPF_6 modification, which suggested that interfacial nonradiative recombination was suppressed (Fig. 5d). Fig. 5e exhibits the V_{OC} as a function of light intensities for the devices based on SnO_2 and KPF_6 -modified SnO_2 . The ideal factor (m) was obtained by fitting the light intensity-dependent V_{OC} curve. The m of the target device was determined to be 1.28, which was much lower than 1.89 of the control devices. It showed that KPF_6 interface modification can effectively inhibit nonradiative recombination, which was in good agreement with TPV result. Electrochemical impedance spectroscopy (EIS) was measured to further evaluate the interfacial carrier transfer and recombination. Fig. 5f shows Nyquist plots of the PSCs based on SnO_2 and SnO_2 with KPF_6 modification which was measured at a bias of 0.9 V in the frequency range of 1 MHz to 0.1 Hz under one sun illumination. The equivalent circuit model in Fig. S8 was utilized to fit the Nyquist plots and the corresponding fitting parameters are exhibited in Table S3. Two obvious semicircle arcs were observed (Fig. 5f). The semicircle arc in the high frequency region was attributed to the charge transfer resistance (R_{ct}) and the semicircle arc in the low frequency region was ascribed to the charge recombination resistance (R_{rec}) [19]. The R_{ct} was reduced from 550 Ω to 502 Ω and R_{rec} was increased from 530 Ω to 843 Ω after KPF_6 modification, indicating that interfacial charge transfer was promoted and interfacial charge recombination was effectively suppressed. In a word, it was successfully demonstrated via different characterization techniques that KPF_6 modification facilitated interfacial charge transfer and suppressed interfacial charge recombination.

Improved interfacial charge extraction and suppressed interfacial charge recombination by KPF_6 modification encouraged us to further investigate the effect of KPF_6 modification on the device performance. The effect of KPF_6 concentrations on device performance was compared (Fig. 6a and Table S4). Obviously, the highest PCE was obtained at the concentration of 0.1 mg/mL. The control device exhibited an average short-circuit current density (J_{SC}) of $22.43 \pm 0.07 \text{ mA/cm}^2$, an average open-circuit voltage (V_{OC}) of $1.093 \pm 0.005 \text{ V}$, an average fill factor (FF) of 0.797 ± 0.004 , and an average PCE of $19.58 \pm 0.12\%$ while the target device based on the optimal concentration of KPF_6 presented an average J_{SC} of $22.92 \pm 0.09 \text{ mA/cm}^2$, an average V_{OC} of $1.128 \pm 0.006 \text{ V}$, an average FF of 0.812 ± 0.002 , and an average PCE of $21.05 \pm 0.15\%$. It was clearly seen that all the photovoltaic parameters were improved after interface modification, due to improved perovskite film quality owing to increased gain size and improved crystallinity, facilitated interfacial charge transfer, released interfacial stress, and reduced interfacial defects from the surface of perovskite film and SnO_2 film, which resulted in reduced nonradiative recombination losses [49]. Both control and target devices exhibited excellent reproducibility, as shown in Fig. 6b and Fig. S9. J-V curves and incident photon to current conversion efficiency (IPCE) spectra of the champion control and target devices are illustrated in Fig. 6c,d. As shown in Table 1, the best-performing control device showed a PCE of 19.66% (corresponding to a J_{SC} of 22.38 mA/cm^2 , a V_{OC} of 1.100 V , and a FF of 0.798) and 19.11% (corresponding to a J_{SC} of 22.27 mA/cm^2 , a V_{OC} of 1.109 V , and a FF of 0.776) in forward scan (FS)

Table 1

Photovoltaic parameters of the best-performing devices without and with KPF_6 modification measured in the reverse scan (RS) and forward scan (FS) under AM 1.5G 1 sun illumination of 100 mW/cm^2 .

Devices	Sweep direction	J_{SC} (mA/cm^2)	V_{OC} (V)	FF	PCE (%)
SnO_2	FS	22.38	1.100	0.798	19.66
	RS	22.27	1.092	0.786	19.11
$\text{SnO}_2/\text{KPF}_6$	FS	22.83	1.145	0.818	21.39
	RS	22.75	1.141	0.813	21.10

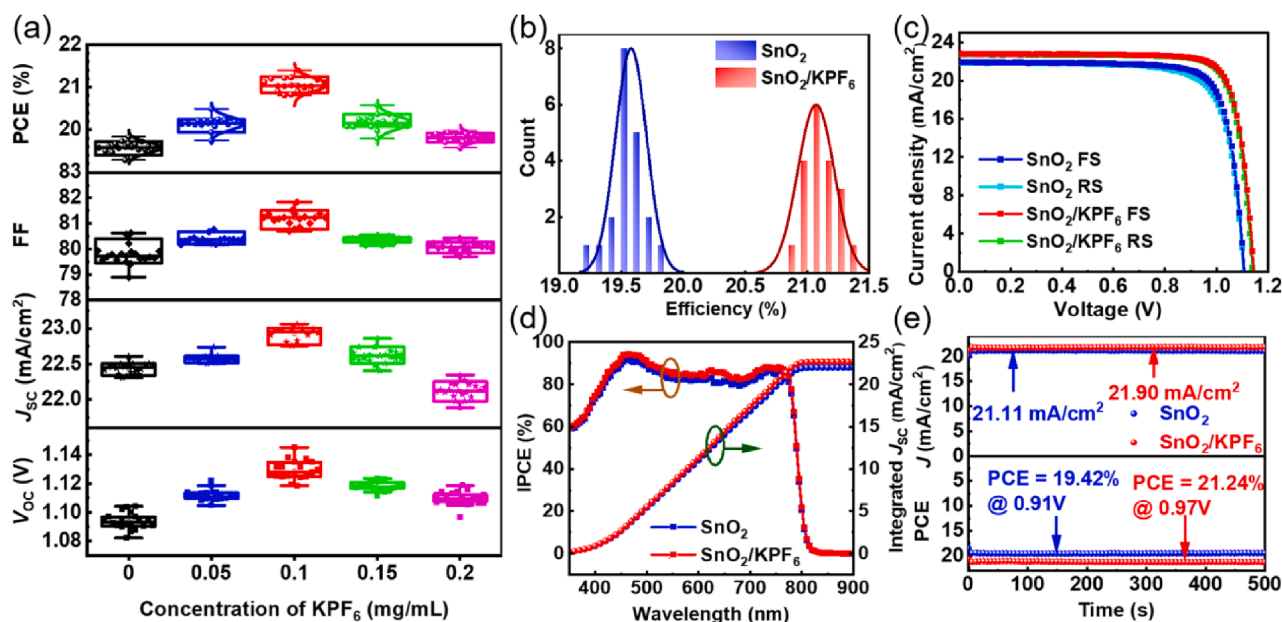


Fig. 6. (a) Statistical distribution diagram of the photovoltaic parameters of the PSCs prepared based on various concentrations of KPF_6 . The statistical data were obtained from 20 individual cells for each kind of device. (b) Statistical distribution of PCEs of the PSCs based on the SnO_2 and SnO_2 modified by KPF_6 of 0.1 mg/mL. The statistical data were obtained from 20 individual cells for each kind of device. (c) J-V curves and (d) corresponding IPCE spectra of the best-performing devices based on SnO_2 and KPF_6 modified SnO_2 . J-V curves were measured in the reverse scan (RS) and forward scan (FS) at a scan rate of 100 mV/s under simulated AM 1.5G one sun illumination of 100 mW/cm^2 . (e) Steady-state current density and PCE versus time for the best-performing devices employing SnO_2 and KPF_6 modified SnO_2 measured at the maximum power point.

and reverse scan (RS), respectively. By contrast, the best-performing target device delivered a PCE of 21.39% (corresponding to a J_{SC} of 22.83 mA/cm², a V_{OC} of 1.145 V, and a FF of 0.818) and 21.10% (corresponding to a J_{SC} of 22.75 mA/cm², a V_{OC} of 1.141 V, and a FF of 0.813) in FS and RS, respectively. A small hysteresis was observed in both kind of devices but the hysteresis was reduced after KPF₆ modification. The interfacial charge accumulation and ion migration have been considered to be main reasons for notorious hysteresis [10,11,50]. In our work, it was inferred that suppressed hysteresis could be due to the improved interfacial charge transfer and thus reduced interfacial charge accumulation as well as suppressed ion migration. As we discussed previously, halide ion migration induced by halide ion vacancies could be inhibited by filling the halide ion vacancies with PF₆⁻ and the organic cation migration also could be suppressed through the hydrogen bond interaction between PF₆⁻ and organic cation. A slightly increased IPCE intensity in the wavelength range of 450–750 nm was found in the target device as compared to the control device, which was put down to the improved interfacial charge transfer and charge collection efficiency along with slightly increased UV-vis absorption intensity (Fig. 6d). The integrated current densities of the control and target devices were 22.02 mA/cm² and 22.70 mA/cm², respectively, which matched well with those from $J-V$ measurement. Fig. 6e illustrates the stable output current density and PCE versus time of the control and target devices measured at maximum power point. The control device gave an output current density of 21.11 mA/cm² and output PCE of 19.42% after 500 s while the target device produced an output current density of 21.90 mA/cm² and output PCE of 21.24% after the same time.

Since the long-term stability is very key to the final commercial application, we investigated the effect of KPF₆ on device stability. The moisture stability of the unencapsulated control and target devices aged under 15%-20% relative humidity at room temperature in the dark are shown in Fig. 7a and Fig. S10. 85.1% of its initial PCE was maintained for the control device after aging for 1440 h while up to 94.7% for the target device under the same aging time. Fig. 7b and Fig. S11 exhibit the thermal stability of the unencapsulated control and target devices aged

at 60 °C in the dark in the nitrogen-filled glovebox. The target device retained 80.1% of its original efficiency after aging for 960 h whereas only 33.2% for the control device. As presented in the photostability in Fig. 7c and Fig. S12, the control device degraded by 80.9% after aging for 960 h while the target device degraded by only 42.8%. It was reported that released interfacial residual stress can improve device stability [38–40]. Ion migration was reported to be one of important reasons for device degradation [10,11,51]. It was revealed that the degradation of PSCs preferentially occurs at the surface and grain boundaries (GBs) of perovskite films since a large amount of defects usually exist at the surface and GBs of perovskite films [10,11,13,14,17]. Consequently, reduced GB density, reduced interfacial defects and improved interfacial contact should be mainly responsible for the increased stability. In addition, we speculated that suppressed halide or cation migration by PF₆⁻ could partially contribute to enhanced stability.

3. Conclusions

In conclusion, we have successfully developed a multifunctional KPF₆ molecule to modify SnO₂/perovskite interface. It is demonstrated that PF₆⁻ is still located at interface while most of K⁺ ions diffuse into perovskite layer. PF₆⁻ can chemically link SnO₂ ETL and perovskite layer via the hydrogen bond with perovskites and coordination bond with ETL, leading to improved interfacial contact. After KPF₆ interface modification, perovskite film quality is improved, interfacial defects are effectively passivated, and interfacial stress is released. As a result, the device with KPF₆ interface modification achieves a higher PCE of 21.39% as compared to the control device (19.66%). Furthermore, the device stability is improved after interface modification. The unencapsulated KPF₆-modified device maintains 80.1% of its initial PCE after aging for 960 h at 60 °C and 57.2% after aging for 960 h under one sun illumination. This work provides a guidance for the design and development of multifunctional interface molecules for the sake of simultaneous enhancement of efficiency and stability of PSCs.

4. Experimental section

Materials: The SnO₂ colloid precursor was obtained from Alfa Aesar (tin (IV) oxide, 15% in H₂O colloidal dispersion). KPF₆ (99%) was brought from Innochem. Lead (II) iodide (PbI₂, 99.99%), and methylamine hydrochloride (MACl, 99.5%) were purchased from Xi'an Polymer Light Technology Corp. Rubidium iodide (RbI, 99.9%) was purchased from Aladdin. Lead (II) bromide (PbBr₂, 99.999%), Formamidine Hydroiodide (FAI, 99.9%), *tert*-butylpyridine (*t*BP, 99%), bis (trifluoromethane) sulfonimide lithium salt (Li-TFSI, 99%), and Spiro-OMeTAD (99.86%) were purchased from Advanced Electron Technology Co. ltd. Methylammonium bromide (MABr) was obtained from GreatCell Solar. *N,N*-dimethylformamide (DMF, 99.8%), dimethylsulphoxide (DMSO, 99.9%), and chlorobenzene (CB, 99.8%) were bought from Sigma Aldrich. All chemical reagents were used as received without further purification.

Device Fabrication: The etched ITO glass was cleaned using a detergent for 10 min, deionized water for 20 min, and ethanol for 20 min, sequentially. Then, the ITO was treated by ultraviolet ozone (UVO) for 20 min. The SnO₂ colloidal solution was prepared by diluting SnO₂ colloidal solution to 2.14 wt% with deionized water. The SnO₂ colloidal solution was spin-coated on the ITO substrates at 4000 rpm for 30 s and then the SnO₂ film was annealed at 150 °C for 30 min. SnO₂ film was exposed to UVO for 10 min. For KPF₆-modified SnO₂, different concentrations of KPF₆ (0.05, 0.1, 0.15, and 0.2 mg/mL) were spin-coated on the cooled SnO₂ films 5000 rpm for 30 s, and then annealed at 100 °C for 10 min. The 1.5 M perovskite precursor solution was prepared by dissolving FAI (232.8 mg), MABr (8.0 mg), RbI (5.9 mg), MACl (36 mg), PbI₂ (656.9 mg), and PbBr₂ (27.5 mg) in the mixed solvents of DMF and DMSO ($V_{DMF}:V_{DMSO} = 8:1$). The perovskite films were prepared by spin-coating the above perovskite precursor solution on the SnO₂ films at

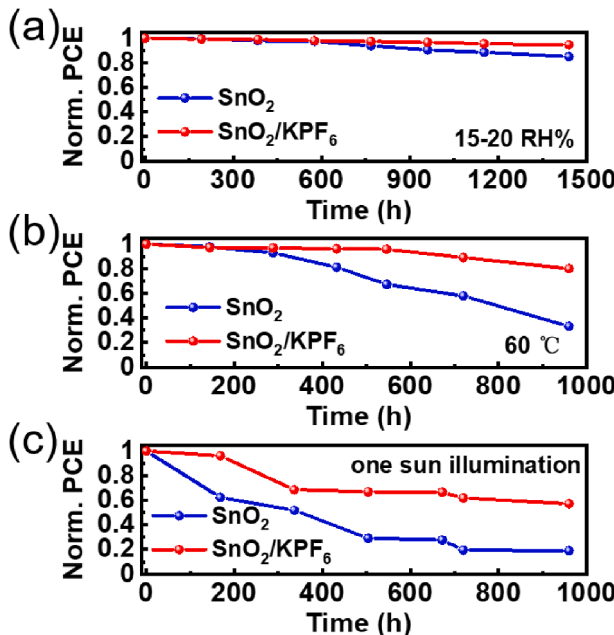


Fig. 7. PCE evolution of the unencapsulated devices based on SnO₂ without and with KPF₆ modification (a) under 15%-20% relative humidity at room temperature in the dark, (b) at 60 °C in the dark in the nitrogen-filled glovebox, and (c) under one sun illumination at room temperature in the nitrogen-filled glovebox. $J-V$ curves were measured in FS at a scan rate of 100 mV/s under simulated AM 1.5G one sun illumination of 100 mW/cm².

4000 rpm for 30 s, in which CB of 80 μL was dripped on perovskite films at 14 s before ending the program, followed by thermal annealing at 155 °C for 23 min. Spiro-OMeTAD solution was prepared by dissolving 72.3 mg of Spiro-OMeTAD, 28.8 μL of tBP, and 17.5 μL of Li-TFSI (520 mg Li-TFSI in 1 mL acetonitrile) in 1 mL CB. Subsequently, hole transport layer was prepared through spin-coating the Spiro-OMeTAD solution on the as-prepared perovskite films for 4000 rpm for 30 s. Finally, an 80 nm gold counter electrode was thermally evaporated on the top of Spiro-OMeTAD film under a vacuum of 3×10^{-4} Pa by using a shadow mask.

Characterizations: XRD and grazing incidence X-ray diffraction (GIXRD) patterns were collected using a PANalytical Empyrean diffractometer equipped with a Cu K α radiation ($\lambda = 1.54056$ Å). XPS measurements were performed on a Thermo-Fisher ESCALab 250Xi system with a monochromatized Al K α (for XPS mode) under the pressure of 5.0×10^{-7} Pa. PL Mapping were recorded by Raman (LabRAM HR Evolution) under the excitation of 532 nm. J-V curves were measured using a solar simulator equipped with a 150 W Xenon lamp (150 W, SolarIV-150A) and a Keithley 2400 source meter. Light intensity was calibrated to AM 1.5G one sun (100 mW/cm 2) with a NIM calibrated standard Si solar cell (QE-B1). The effective active area of the device was defined to be 0.07 cm 2 by using a black metal mask. J-V curves were measured from -0.1 V to 1.2 V (forward scan, FS) or from 1.2 V to -0.1 V (reverse scan, RS) with a scan rate of 100 mV/s. The incident photon-to-electron conversion efficiency (IPCE) measurement was conducted on an IPCE measurement system. UV-vis absorption measurement was carried out on a Shimadzu UV-1800 spectrophotometer. SEM images were collected using JSM-7800F. The FTIR spectra were recorded with a Nicolet iS50 Infrared Fourier transform microscope by Thermo Fisher Scientific. Time-resolved photoluminescence (TRPL) and steady-state photoluminescence (SSPL) spectra were measured using Edinburgh FLS1000, where the excitation wavelength of TRPL was provided by a 450 nm laser. Atomic force microscopy (AFM) measurement was performed on Asylum Research MFP-3D-BIO in tapping mode. TPV and TPC measurements were performed as follows: the devices were illuminated by laser pulses (532 nm, 100 mJ, 6 ns width from an Nd:YAG laser), and then the decay of signals was recorded by a 1 GHz Agilent digital oscilloscope (DSO-X3102A) with the input impedance of 1 M Ω /50 Ω. Impedance spectroscopy was measured by an Electrochemical Workstation. Time-of-flight secondary ion mass spectrometry (ToF-SIMS) measurement was carried out using a dual-beam TOF-SIMS IV (IONTOF) spectrometer equipped with a 30 keV, 1 pA Bi $^{+}$ beam for the analysis and a 1 keV, 1 nA O $^{2-}$ ion beam for the sputtering operated in noninterlaced mode.

Declaration of Competing Interest

The authors declare that they have no known competing financial interests or personal relationships that could have appeared to influence the work reported in this paper.

Acknowledgements

This work was financially supported by the Fundamental Research Funds for the Central Universities (Grant Nos. 2020CDJQY-A028, 2020CDJ-LHZZ-074), Natural Science Foundation of Chongqing (Grant No. cstc2020jcyj-msxmX0629), Support plan for Overseas Students to Return to China for Entrepreneurship and Innovation (Grant No. cx2020003), Henan Ed Era New Energy Science & technology Co., Ltd (Grant No. H20200282), and research start-up fund of Chongqing University (Grant No. 02100011044126). We would like to thank Analytical and Testing Center of Chongqing University for various measurements.

Appendix A. Supplementary data

Supplementary data to this article can be found online at <https://doi.org/10.1016/j.cej.2021.129375>.

<https://doi.org/10.1016/j.cej.2021.129375>.

References

- [1] H.-S. Kim, C.-R. Lee, J.-H. Im, K.-B. Lee, T. Moehl, A. Marchioro, S.-J. Moon, R. Humphry-Baker, J.-H. Yum, J.E. Moser, M. Grätzel, N.-G. Park, Lead iodide perovskite sensitized all-solid-state submicron thin film mesoscopic solar cell with efficiency exceeding 9%, *Sci. Rep.* 2 (2012) 591.
- [2] NREL, Best research-cell efficiency chart, 2020. <https://www.nrel.gov/pv/assets/pdfs/best-research-cell-efficiencies.20200925.pdf>.
- [3] M. Kim, G.-H. Kim, T.K. Lee, I.W. Choi, H.W. Choi, Y. Jo, Y.J. Yoon, J.W. Kim, J. Lee, D. Huh, H. Lee, S.K. Kwak, J.Y. Kim, D.S. Kim, Methylammonium chloride induces intermediate phase stabilization for efficient perovskite solar cells, *Joule* 3 (2019) 2179–2192.
- [4] H. Min, M. Kim, S.-U. Lee, H. Kim, G. Kim, K. Choi, J.H. Lee, S.I. Seok, Efficient, stable solar cells by using inherent bandgap of α -phase formamidinium lead iodide, *Science* 366 (2019) 749–753.
- [5] M. Jeong, I.W. Choi, E.M. Go, Y. Cho, M. Kim, B. Lee, S. Jeong, Y. Jo, H.W. Choi, J. Lee, Stable perovskite solar cells with efficiency exceeding 24.8% and 0.3V voltage loss, *Science* 369 (2020) 1615–1620.
- [6] Y. Chen, S. Tan, N. Li, B. Huang, X. Niu, L. Li, M. Sun, Y.u. Zhang, X. Zhang, C. Zhu, N. Yang, H. Zai, Y. Wu, S. Ma, Y. Bai, Q.i. Chen, F. Xiao, K. Sun, H. Zhou, Self-elimination of intrinsic defects improves the low-temperature performance of perovskite photovoltaics, *Joule* 4 (2020) 1961–1976.
- [7] H. Wang, H. Wang, S. Chen, B. Zhang, G. Yang, P. Gao, J. Liu, X. Fan, Y. Huang, J. Lin, Z. Shen, A depth-profiling study on the solid electrolyte interface: bis (fluorosulfuryl)imide anion toward improved K $^{+}$ storage, *ACS Appl. Energy Mater.* 2 (2019) 7942–7951.
- [8] Q. Jiang, Y. Zhao, X. Zhang, X. Yang, Y. Chen, Z. Chu, Q. Ye, X. Li, Z. Yin, J. You, Surface passivation of perovskite film for efficient solar cells, *Nat. Photonics* 13 (2019) 460–466.
- [9] S. You, H. Zeng, Z. Ku, X. Wang, Z. Wang, Y. Rong, Y. Zhao, X. Zheng, L. Luo, L. Li, Multifunctional polymer-regulated SnO₂ nanocrystals enhance interface contact for efficient and stable planar perovskite solar cells, *Adv. Mater.* 32 (2020) 2003990.
- [10] J. Chen, N.G. Park, Causes and solutions of recombination in perovskite solar cells, *Adv. Mater.* 31 (2019) 1803019.
- [11] J. Chen, N.-G. Park, Materials and methods for interface engineering toward stable and efficient perovskite solar cells, *ACS Energy Lett.* 5 (2020) 2742–2786.
- [12] H.-S. Kim, N.-G. Park, Importance of tailoring lattice strain in halide perovskite crystals, *NPG Asia Mater.* 12 (2020) 78.
- [13] L.K. Ono, S.F. Liu, Y. Qi, Reducing detrimental defects for high-performance metal halide perovskite solar cells, *Angew. Chem. Int. Ed.* 59 (2020) 6676.
- [14] B.O. Chen, P.N. Rudd, S. Yang, Y. Yuan, J. Huang, Imperfections and their passivation in halide perovskite solar cells, *Chem. Soc. Rev.* 48 (2019) 3842–3867.
- [15] A.A. Said, J. Xie, Q. Zhang, Recent progress in organic electron transport materials in inverted perovskite solar cells, *Small* 15 (2019) 1900854.
- [16] P.-Y. Gu, N. Wang, A. Wu, Z. Wang, M. Tian, Z. Fu, X.W. Sun, Q. Zhang, An azacene derivative as promising electron-transport layer for inverted perovskite solar cells, *Chem. Asian J.* 11 (2016) 2135–2138.
- [17] C. Ran, J. Xu, W. Gao, C. Huang, S. Dou, Defects in metal triiodide perovskite materials towards high-performance solar cells: origin, impact, characterization, and engineering, *Chem. Soc. Rev.* 47 (2018) 4581–4610.
- [18] P. Zhu, S. Gu, X. Luo, Y. Gao, S. Li, J. Zhu, H. Tan, Simultaneous contact and grain-boundary passivation in planar perovskite solar cells using SnO₂-KCl composite electron transport layer, *Adv. Energy Mater.* 10 (2020) 1903083.
- [19] J. Chen, X. Zhao, S.G. Kim, N.G. Park, Multifunctional chemical linker imidazoleacetic acid hydrochloride for 21% efficient and stable planar perovskite solar cells, *Adv. Mater.* 31 (2019) 1902902.
- [20] K. Liu, S. Chen, J. Wu, H. Zhang, M. Qin, X. Lu, Y. Tu, Q. Meng, X. Zhan, Fullerene derivative anchored SnO₂ for high-performance perovskite solar cells, *Energy Environ. Sci.* 11 (2018) 3463–3471.
- [21] G. Yang, C. Wang, H. Lei, X. Zheng, P. Qin, L. Xiong, X. Zhao, Y. Yan, G. Fang, Interface engineering in planar perovskite solar cells: energy level alignment, perovskite morphology control and high performance achievement, *J. Mater. Chem. A* 5 (2017) 1658–1666.
- [22] L. Zuo, Q.i. Chen, N. De Marco, Y.-T. Hsieh, H. Chen, P. Sun, S.-Y. Chang, H. Zhao, S. Dong, Y. Yang, Tailoring the interfacial chemical interaction for high-efficiency perovskite solar cells, *Nano Lett.* 17 (2017) 269–275.
- [23] J. Wang, K. Datta, C.H. Weijtens, M.M. Wienk, R.A. Janssen, Insights into fullerene passivation of SnO₂ electron transport layers in perovskite solar cells, *Adv. Funct. Mater.* 29 (2019) 1905883.
- [24] M. Zhong, Y. Liang, J. Zhang, Z. Wei, Q. Li, D. Xu, Highly efficient flexible MAPbI₃ solar cells with a fullerene derivative-modified SnO₂ layer as the electron transport layer, *J. Mater. Chem. A* 7 (2019) 6659–6664.
- [25] Z. Li, L. Wang, R. Liu, Y. Fan, H. Meng, Z. Shao, G. Cui, S. Pang, Spontaneous interface ion exchange: passivating surface defects of perovskite solar cells with enhanced photovoltaic, *Adv. Energy Mater.* 9 (2019) 1902142.
- [26] K. Choi, J. Lee, H.I. Kim, C.W. Park, G.-W. Kim, H. Choi, S. Park, S.A. Park, T. Park, Thermally stable, planar hybrid perovskite solar cells with high efficiency, *Energy Environ. Sci.* 11 (2018) 3238–3247.
- [27] D. Zheng, R. Peng, G. Wang, J.L. Logsdon, B. Wang, X. Hu, Y. Chen, V.P. Dravid, M. R. Wasieleski, J. Yu, Simultaneous bottom-up interfacial and bulk defect passivation in highly efficient planar perovskite solar cells using nonconjugated small-molecule electrolytes, *Adv. Mater.* 31 (2019) 1903239.

- [28] X. Liu, Y. Zhang, L. Shi, Z. Liu, J. Huang, J.S. Yun, Y. Zeng, A. Pu, K. Sun, Z. Hameiri, Exploring inorganic binary alkaline halide to passivate defects in low-temperature-processed planar-structure hybrid perovskite solar cells, *Adv. Energy Mater.* 8 (2018), 1800138.
- [29] Z. Tang, S. Uchida, T. Bessho, T. Kinoshita, H. Wang, F. Awai, R. Jono, M. Maitani, J. Nakazaki, T. Kubo, H. Segawa, Modulations of various alkali metal cations on organometal halide perovskites and their influence on photovoltaic performance, *Nano Energy* 45 (2018) 184–192.
- [30] D.-Y. Son, S.-G. Kim, J.-Y. Seo, S.-H. Lee, H. Shin, D. Lee, N.-G. Park, Universal approach toward hysteresis-free perovskite solar cell via defect engineering, *J. Am. Chem. Soc.* 140 (2018) 1358–1364.
- [31] M. Abdi-Jalebi, Z. Andaji-Garmaroudi, S. Cacovich, C. Stavrakas, B. Philippe, J. M. Richter, M. Alsari, E.P. Booker, E.M. Hutter, A.J. Pearson, S. Lilliu, T.J. Savenije, H. Rensmo, G. Divitini, C. Ducati, R.H. Friend, S.D. Stranks, Maximizing and stabilizing luminescence from halide perovskites with potassium passivation, *Nature* 555 (2018) 497–501.
- [32] F. Zheng, W. Chen, T. Bu, K.P. Ghiggino, F. Huang, Y. Cheng, P. Tapping, T.W. Kee, B. Jia, X. Wen, Triggering the passivation effect of potassium doping in mixed-cation mixed-halide perovskite by light illumination, *Adv. Energy Mater.* 9 (2019), 1901016.
- [33] J. Chen, S.G. Kim, N.G. Park, $\text{FA}_{0.88}\text{Cs}_{0.12}\text{PbI}_{3-x}(\text{PF}_6)_x$ interlayer formed by ion exchange reaction between perovskite and hole transporting layer for improving photovoltaic performance and stability, *Adv. Mater.* 30 (2018) 1801948.
- [34] D. Yang, X. Zhou, R. Yang, Z. Yang, W. Yu, X. Wang, C. Li, S. Liu, R.P.H. Chang, Surface optimization to eliminate hysteresis for record efficiency planar perovskite solar cells, *Energy Environ. Sci.* 9 (2016) 3071–3078.
- [35] S. Yang, S. Chen, E. Mosconi, Y. Fang, X. Xiao, C. Wang, Y.u. Zhou, Z. Yu, J. Zhao, Y. Gao, F. De Angelis, J. Huang, Stabilizing halide perovskite surfaces for solar cell operation with wide-bandgap lead oxysalts, *Science* 365 (2019) 473–478.
- [36] J. Dagar, K. Hirselundt, A. Merdasa, A. Czudek, R. Munir, F. Zu, N. Koch, T. Dittrich, E.L. Unger, Alkali salts as interface modifiers in n-i-p hybrid perovskite solar cells, *Sol. RRL* 3 (2019), 1900088.
- [37] J. Zheng, J. Chen, D. Ouyang, Z. Huang, X. He, J. Kim, W.C.H. Choy, Critical role of functional groups in defect passivation and energy band modulation in efficient and stable inverted perovskite solar cells exceeding 21% efficiency, *ACS Appl. Mater. Interfaces* 12 (2020) 57165–57173.
- [38] D.-J. Xue, Y. Hou, S.-C. Liu, M. Wei, B. Chen, Z. Huang, Z. Li, B. Sun, A.H. Proppe, Y. Dong, Regulating strain in perovskite thin films through charge-transport layers, *Nat. Commun.* 11 (2020) 1–8.
- [39] H. Wang, C. Zhu, L. Liu, S. Ma, P. Liu, J. Wu, C. Shi, Q. Du, Y. Hao, S. Xiang, Interfacial residual stress relaxation in perovskite solar cells with improved stability, *Adv. Mater.* 31 (2019), 1904408.
- [40] Q. Zhou, J. Duan, X. Yang, Y. Duan, Q. Tang, Interfacial strain release from the $\text{WS}_2/\text{CsPbBr}_3$ van der waals heterostructure for 1.7V voltage all-inorganic perovskite solar cells, *Angew. Chem. Int. Ed.* 132 (2020) 22181–22185.
- [41] D. Shuttleworth, Preparation of metal-polymer dispersions by plasma techniques. An ESCA investigation, *J. Phys. Chem.* 84 (1980) 1629–1634.
- [42] C. Lee, W.-Y. Lee, H. Lee, S. Ha, J.-H. Bae, I.-M. Kang, H. Kang, K. Kim, J. Jang, Sol-gel processed yttrium-doped SnO_2 thin film transistors, *Electron.* 9 (2020) 254.
- [43] I. Wharf, D.F. Shriver, Vibrational frequencies and intramolecular forces in anionic tin-halogen complexes and related species, *Inorg. Chem.* 8 (1969) 914–925.
- [44] S.S. Mali, J.V. Patil, H. Arandian, C.K. Hong, Reduced methylammonium triple-cation $\text{Rb}_{0.05}(\text{FAPbI}_3)_{0.95}(\text{MAPbBr}_3)_{0.05}$ perovskite solar cells based on a $\text{TiO}_2/\text{SnO}_2$ bilayer electron transport layer approaching a stabilized 21% efficiency: the role of antisolvents, *J. Mater. Chem. A* 7 (2019) 17516–17528.
- [45] R. Takouachet, R. Benali-Cherif, E.-E. Bendeif, N. Benali-Cherif, S. Pillet, D. Schaniel, Structural analysis and IR-spectroscopy of a new anilinium hydrogenselenite hybrid compound: A subtle structural phase transition, *Inorg. Chim. Acta* 446 (2016) 6–12.
- [46] J. Chen, S.-G. Kim, X. Ren, H.S. Jung, N.-G. Park, Effect of bidentate and tridentate additives on the photovoltaic performance and stability of perovskite solar cells, *J. Mater. Chem. A* 7 (2019) 4977–4987.
- [47] K. Chen, Q. Hu, T. Liu, L. Zhao, D. Luo, J. Wu, Y. Zhang, W. Zhang, F. Liu, T. P. Russell, R. Zhu, Q. Gong, Charge-carrier balance for highly efficient inverted planar heterojunction perovskite solar cells, *Adv. Mater.* 28 (2016) 10718–10724.
- [48] Y. Zheng, R. Su, Z. Xu, D. Luo, H. Dong, B. Jiao, Z. Wu, Q. Gong, R. Zhu, Perovskite solar cell towards lower toxicity: a theoretical study of physical lead reduction strategy, *Sci. Bull.* 64 (2019) 1255–1261.
- [49] D. Luo, R. Su, W. Zhang, Q. Gong, R. Zhu, Minimizing non-radiative recombination losses in perovskite solar cells, *Nat. Rev. Mater.* 5 (2020) 44–60.
- [50] D.H. Kang, N.G. Park, On the current–voltage hysteresis in perovskite solar cells: dependence on perovskite composition and methods to remove hysteresis, *Adv. Mater.* 31 (2019) 1805214.
- [51] Y. Yuan, J. Huang, Ion Migration in organometal trihalide perovskite and its impact on photovoltaic efficiency and stability, *Acc. Chem. Res.* 49 (2016) 286–293.